

Elastic turbulence in a curvilinear channel flow

Yonggun Jun and Victor Steinberg

Department of Physics of Complex Systems, Weizmann Institute of Science, Rehovot, IL-76100 Israel

(Received 19 August 2011; published 28 November 2011)

We report detailed quantitative studies of elastic turbulence in a curvilinear channel flow in a dilute polymer solution of high molecular weight polyacrylamide in a high viscosity water-sugar solvent. Detailed studies of the average and rms velocity and velocity gradients profiles reveal the emergence of a boundary layer associated with the nonuniform distribution of the elastic stresses across the channel. The characteristic boundary width is independent of the Weissenberg number Wi and proportional to the channel width, which is consistent with the findings our early investigations of the boundary layer in elastic turbulence in different flow geometries. The nonuniform distribution of the elastic stresses across the channel and appearance of the characteristic spatial scales of the order of the boundary layer width of both velocity and velocity gradient in the correlation functions of the velocity and velocity gradient fields in a bulk flow may suggest that excessive elastic stresses, concentrated in the boundary layer, are ejected into the bulk flow similar to jets observed in passive scalar mixing in elastic turbulence observed recently. Finally, the experimental results show that one of the main predictions of the theory of elastic turbulence, namely, the saturation of the normalized rms velocity gradient in the bulk flow of elastic turbulence contradicts the experimental observations both qualitatively and quantitatively in spite of the fact that the theory explains well the observed sharp power-law decay of the velocity power spectrum. The experimental findings call for further development of theory of elastic turbulence in a bounded container, similar to what was done for a passive scalar problem.

DOI: [10.1103/PhysRevE.84.056325](https://doi.org/10.1103/PhysRevE.84.056325)

PACS number(s): 47.20.Gv, 47.50.-d, 47.27.-i

I. INTRODUCTION

The addition of small amount of long polymer molecules into a fluid makes it elastic and capable of storing elastic stresses that may strongly alter flow properties [1]. First of all, the elastic stresses generated by the polymer stretching in the flow becomes the main source of nonlinearity in the polymer solution flow at low Reynolds numbers (Re). As a result, an elastic instability shows up when the elastic energy overcomes the dissipation due to polymer relaxation. The ratio of the nonlinear elastic term to the linear relaxation is defined by the Weissenberg number Wi [1], which is the main control parameter in the problem, and the elastic instability occurs in a shear flow with curvilinear trajectories at $Wi_c \geq 1$. Above the purely elastic instability, a path to a chaotic flow in a form of irregular flow patterns at $Wi > Wi_c$ was studied in three flow geometries: Couette flow between cylinders, von Karman swirling flow between two disks, and flow in a curvilinear channel [2–4]. Further increase of Wi at vanishingly small Re leads to the most remarkable phenomenon discovered recently experimentally [2] and then studied during the last decade in an increasing number of experimental [3–8] and theoretical [9–12] papers, namely “elastic turbulence.” It is spatially smooth and random in time flow, which is driven by strong polymer stretching and resulting elastic stresses and is observed at sufficiently large Wi and at vanishingly small Re . Many properties of the elastic turbulence regime, namely, statistics of velocity and velocity gradient fields, spatial and temporal velocity correlation functions and power-law behavior of velocity power spectrum, a new length scale (the boundary layer width and its properties), scaling, and statistical properties of torque and pressure fluctuations, were observed and investigated experimentally in von Karman swirling flow between two disks and only a few of them theoretically and numerically [7].

On the other hand, a detailed description of similar properties in a channel flow is lacking, though elastic turbulence in a curvilinear channel was used to demonstrate its effectiveness in mixing in macro- as well as in microchannels [3–5,13,14]. In a 3 mm^2 square cross-section curvilinear channel the longitudinal and transverse flow velocity components were measured by a laser Doppler anemometer at the bend $N = 12$ near the middle of the half-ring at a fixed value of Wi , about twice larger than at the onset of the elastic instability. The power spectra of the longitudinal and transversal velocity components show a broad region of an algebraic decay $f^{-3.3}$ in the frequency domain. The rms of velocity fluctuations were $0.09\langle V \rangle$ and $0.04\langle V \rangle$ for the longitudinal and transverse components, respectively, where $\langle V \rangle$ is the mean longitudinal velocity. Since the power spectra were measured at a point where the mean velocity was more than 10 times higher than its rms value, the Taylor hypothesis could be used to transfer the power-law decay in the frequency domain to the wave-number k domain. Then the measured power-law decay in the frequency spectrum $f^{-3.3}$ gave the wave-number spectrum $k^{-3.3}$, which is very close to the scaling exponent found in the von Karman swirling flow between two disks in both frequency and wave-number domains [2,7]. Other measurements of the flow velocity were carried out in a microchannel of a similar design as the 3-mm channel but scaled down 30 times compared with the macrochannel version [5,13]. In order to define the onset of the elastic instability, both the longitudinal and the transverse velocity field components were measured by microscopic particle image velocimetry (micro-PIV) as a function of the pressure drop Δp along the channel. The resulting flow resistance, defined as $\Delta p/\bar{V}$, as a function of the pressure drop shows sharp but continuous change in the dependence that determines the instability onset. A similar dependence is observed on the plot of V_θ^{rms} as well as V_r^{rms} versus Δp [5,13]. Temporal dependencies of

the longitudinal velocity as well as its correlation function were also measured and the velocity correlation time was determined. By using 0.2- μm fluorescent particles streamwise vortices were visualized by means of horizontal confocal scanning microscopy in the middle plane of the channel [5,13]. In the recent detailed studies of mixing in a curvilinear channel of 1 mm² square cross section using elastic turbulence, some partial characterization of the velocity field necessary for quantitative characterization of mixing, namely, both average $\langle V_r \rangle$ and rms V_r^{rms} radial and $\langle V_\theta \rangle$ and V_θ^{rms} longitudinal velocity profiles across the channel, dependence of $\langle V_\theta \rangle$ on Wi , profiles of rms of longitudinal $\partial V_\theta / \partial r$, and radial $\partial V_r / \partial r$ velocity gradients, was carried out [14].

A theory of elastic turbulence was developed and published in Ref. [15] right away after publication of the experimental results [2]. The main concern of the theory was to explain the key experimental observation in elastic turbulence, namely, the sharp algebraic decay of the velocity power spectrum with the scaling exponent δ between -3.3 and -3.6 [2,3]. Due to the sharp velocity spectrum decay, the velocity and velocity gradient are both determined mostly by the large scale, that is, the vessel size. It means that elastic turbulence is essentially spatially smooth and random in time flow, dominated by nonlinear interaction of a few large-scale modes. It is the same random flow that occurs in hydrodynamic turbulence below the dissipation scale and is called the Batchelor flow regime [16]. It results from stretching and folding of an elastic stress field, similar to the stretching and folding of a passive scalar field in the Batchelor regime of mixing. A crucial difference between elastic turbulence and passive scalar mixing is that in the case of elastic turbulence the corresponding elastic stress field is not passive but reacts back on the driving velocity field and in such way stabilizes the flow [9,15]. There are two aspects of theory of polymer stretching in a flow. First is a description of the statistics of polymer stretching and of a coil-stretch transition in a spatially smooth and random in time flow. The second is a characterization of the properties of elastic turbulence resulting from the polymer stretching.

The first aspect requires a microscopic approach to the problem, which provides a quantitative prediction on the coil-stretch transition of a polymer and on a saturation of the polymer stretching in a spatially isotropic random unbounded flow, as well as a detailed prescription of its experimental verification [17,18]. These predictions were tested experimentally, and good agreement was found [19,20]. The coil-stretch transition has a remarkable macroscopic consequence on a flow: Properties of the polymer solution become essentially non-Newtonian and the stretched polymers significantly alter the flow due to their back reaction. The second aspect, on the other hand, requires a macroscopic description of elastic turbulence, which has been developed by Lebedev *et al.* [9,15] and is based on polymers with linear elasticity and the feedback reaction on the flow. The theory of elastic turbulence uses the set of equations for the elastic stress tensor and velocity fields. Hydrodynamic description of a polymer solution flow and of dynamics of elastic stresses for linear polymers is analogous to that of a small-scale fast dynamo in magneto-hydrodynamics (MHD) and also of turbulent advection of a passive scalar in the Batchelor regime [9,16], though some significant differences exist. The

stretching of the magnetic lines is similar to the polymer stretching, and the difference with MHD lies in the relaxation term that replaces the diffusion term in MHD description, whereas in the passive scalar advection problem the dynamo effect, that is, feedback reaction on the flow, is absent. In all three cases the basic physics is the same, rather general and directly related to the classical Batchelor regime of mixing: stretching and folding of the passive scalar, magnetic, or stress fields by a random advecting flow.

Theory of elastic turbulence in an unbounded flow of a polymer solution is based on the following assumptions [9,15]. (i) A statistically stationary state occurs due to the feedback reaction of stretched polymers (or the elastic stress) on the velocity field that leads to a saturation of the elastic stress σ_p and rms of the velocity gradients $(\partial V_i / \partial x_j)_{\text{rms}}$ [and so $Wi_{\text{loc}} = (\partial V_i / \partial x_j)_{\text{rms}} \lambda$, where λ is the longest polymer relaxation time], even for polymers with linear elasticity [9,15]. The saturation value in a bulk of elastic turbulence is $Wi_{\text{loc}} \simeq 1$ and constant at all Wi above the coil-stretch transition. It is the key theoretical prediction [9,15]. (ii) Both dissipative terms due to viscosity and polymer relaxation, which appear in the equation for the dissipation of elastic energy [15], are of the same order, that is, $\sigma_p / \lambda \sim \eta (\nabla V)^2$ or otherwise $\sigma_p \lambda / \eta \sim Wi_{\text{loc}}^2$, where η is the viscosity. Then both assumptions lead to the following result: The normalized elastic stress $\sigma_p \lambda / \eta \simeq 1$ and also saturates. These two important theoretical predictions deserve a stringent experimental test. Indeed, the value of elastic stresses was measured in the recent experiment in a microscopic arrangement of a swirling flow [21] and strong discrepancy was identified. The first prediction on the saturation of Wi_{loc} in a bulk flow of elastic turbulence was examined in a swirling macroscopic flow [7] and quantitative disagreement was found. On the other hand, the further theoretical analysis leads to a powerlike decaying spatial spectrum for the elastic stresses and for the velocity field fluctuations with the exponent $|\delta| > 3$ in a good accord with the experimental results [2,3]. The close value of the exponent in the velocity power spectra decay was also obtained in the numerical simulations of elastic turbulence based on the Kolmogorov shear flow of a dilute polymer solution described by the Oldroyd-B model [10,11].

In this paper we provide a complete characterization of the channel flow in the elastic turbulence regime and present statistics, correlations and scaling of velocity and velocity gradient fields in the bulk as well as in the vicinity of the wall, and also properties of the velocity gradient boundary layer that provide us the possibility also to further test the theoretical prediction about the saturation of Wi_{loc} .

The paper is organized as follows. In Sec. II, the experimental setup is described in detail. In Sec. III the experimental results are presented. Here we first describe in Sec. III A flow structure and experimental determination of the elastic instability threshold. Then in Sec. III B various velocity and velocity gradient profiles and a determination of the boundary layer widths of velocity and velocity gradient and its functional dependence are described. Temporal and spatial correlation functions of velocity and velocity gradients and correlation times and lengths as a function of Wi are presented in Sec. III C. Finally, statistics of velocity and velocity gradients

and structure function scalings are discussed in Sec. III D. A discussion of the experimental results is given in Sec. IV and conclusions are presented in Sec. V.

II. EXPERIMENTAL SETUP AND PROCEDURE

The experiments were conducted in a curvilinear channel of about 1 mm^2 square cross section machined out of Plexiglas (Lucite). The width size was chosen to reduce by an order of magnitude the amount of a working fluid (polymer solution) used in the first experiment with the channel cross section of 3 mm^2 [3,4] and to increase spatial resolution of a velocity field in peripheral regions compared with the second experiment, where a microchannel of $100 \text{ }\mu\text{m}^2$ square cross section was used [5,13]. The channel used in the current experiment contained 63 pairs of identical smoothly connected half rings (bends or units) with inner and outer radii of $R_i = 1 \text{ mm}$ and $R_o = 2 \text{ mm}$, respectively, and sufficiently high gap ratio $d/R_i = 1$, the same as in the previous experiment [14], which was intended to facilitate the onset of the elastic instability at sufficiently low Wi . Here $d = R_o - R_i$ is the channel width. The precise dimensions of the channel were 0.95 mm width at the midplane of the channel, where measurements of mixing were performed (with $\pm 0.05\text{-}\mu\text{m}$ differences in the width at the top and bottom of the channel), and 1.025 mm depth. Thus, the entire channel length was approximately 59.4 cm measured along a channel midplane (see Fig. 1). The channel main body and the lid were squeezed between two stainless steel plates to seal the channel with an O-ring against leaks and to preserve a flatness along the channel.

The pulse Nd-YAG laser of the 532 nm wavelength (New Wave Research Ltd.), which produced pulses of power $30 \text{ mJ}/5 \text{ ns}$ with time delay between the pulses of $10 \text{ }\mu\text{s}$, was used to conduct particle image velocimetry (PIV) measurements. Time differences between two consecutive images were chosen depending on Wi between 0.51 and 1.84 ms , and laser pulses and the camera were synchronized via the control units of the PIV laser system. For visualization of velocity field measurements, red fluorescent particles (Duke Scientific Ltd.) of $2 \text{ }\mu\text{m}$ at concentration of 150 ppm were used. As in the previous setups [3,4,14], the channel was illuminated from the side by a laser beam transformed by an appropriate optical setup containing two cylindrical lenses

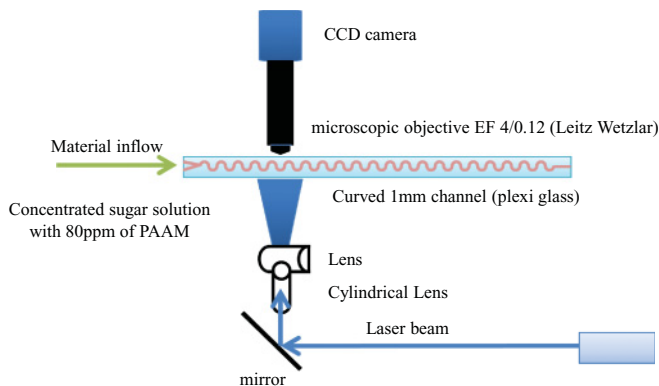


FIG. 1. (Color online) Schematic drawing of the experimental setup.

to a broad light sheet of a thickness about $\sim 50 \text{ }\mu\text{m}$ in the observation region (see Fig. 1). A thinner light sheet causes a permanent damage to Plexiglas. The laser beam sheet produced a thin cut in the three-dimensional (3D) flow, parallel to the top and bottom of the channel at its midplane. Fluorescent light emitted by the particles in the direction perpendicular to the beam plane was detected by a charge coupled device (CCD) via a microscope objective EF 4.0/0.12 (Leitz Wetzlar) mounted on the plastic tube (guide). The CCD camera Grasshopper, Model Gras-1455M-C (Grey Point Research), of 16-bit grayscale resolution and with spatial resolution of 1280×768 pixels at up to 30 frames/s rate was used. Together with the microscope objective, it provided a PIV spatial resolution of $0.576 \text{ }\mu\text{m}/\text{pixel}$. The size of the PIV image was 1280×384 pixels. The window size to get velocity vectors was taken at 32×8 pixels, which corresponded to $18.4 \times 4.6 \text{ }\mu\text{m}^2$. A total of 130 velocity vectors in the transverse direction to the flow were obtained from PIV. Thus, the velocity gradients were calculated on a $dr = 4.6 \text{ }\mu\text{m}$ step. The images were taken at a rate of 10 fps . Since each two consecutive images were transformed into one velocity field, the final rate of the velocity field sampling was 5 Hz . A total of 1000 velocity fields were used for averaging.

The velocity profile in the channel flow of the Newtonian solvent measured by PIV has been used for calibration. Figure 2 presents the results of longitudinal velocity profiles $V_\theta(r/d)$ across the channel in a laminar flow of the solvent for various pressure drops. (We use in the channel middle plane the coordinates z and r as longitudinal and transversal to the channel walls, respectively, and V_θ and V_r as the longitudinal and radial components of the velocity field, respectively.) We visualize just a part of the channel cross section to increase a spatial resolution, since later on we use only the velocity maximum values and the velocities in a peripheral region close to the wall. Due to curvature in serpentine geometry of the channel, the profiles of the longitudinal velocity are not symmetric relative to the middle plane, in contrast to a straight channel. Figure 3 shows a linear dependence of the maximum values of the velocity profiles V_θ^{max} (or the

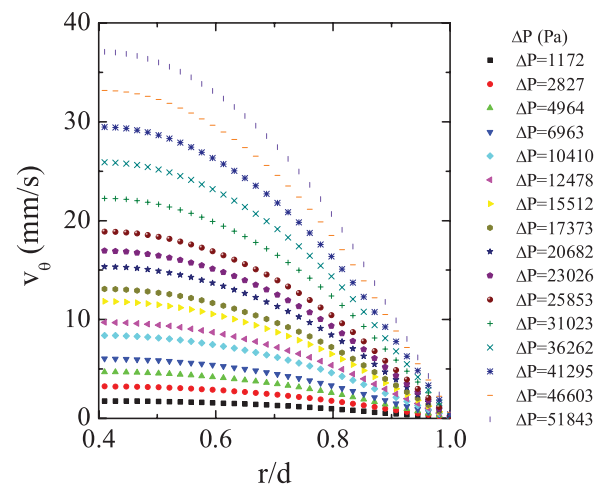


FIG. 2. (Color online) Longitudinal velocity profiles across a channel of a solvent laminar flow in a curvilinear channel at various pressure drops (starting from small values at bottom to top; $r = 0$ corresponds to the inner channel wall).

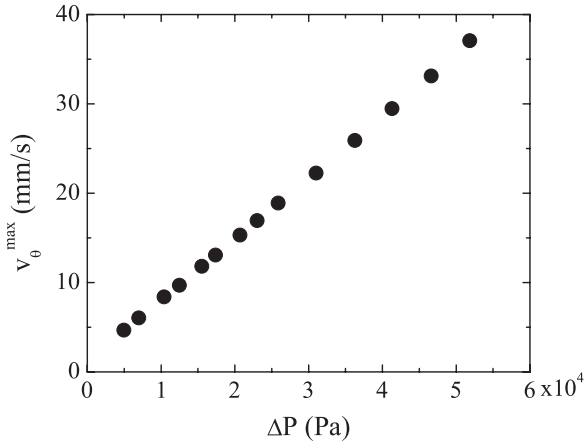


FIG. 3. Maximum velocity profile versus pressure drop along the channel ΔP for the solvent of water with 65% sucrose in a laminar channel flow.

discharge) in a laminar flow of the solvent as a function of the pressure drop ΔP along the channel, which is used for calibration.

As a working fluid, a 65% sucrose-water solvent with addition of 1% NaCl, 250 ppm of NaN_3 , and 80 ppm by weight high molecular weight polyacrylamide (PAAm) ($M_w = 18$ Mda, supplied by Polysciences), was used. It was prepared from a master water solution contained 3000 ppm of PAAm, 1% NaCl, 250 ppm of NaN_3 , and 3% of iso-propanol [14]. The viscosities of the solvent $\eta_s = 113.8$ mPa · s and the polymer solution $\eta = 137.6$ mPa · s were measured at 22 ± 0.5 °C, the same temperature kept during the experiment. The longest polymer relaxation time measured by the stress relaxation method was $\lambda = 11.5$ s and was found to be independent of the shear rate [21] (it differs from values used in Refs. [5,13], where the polymer relaxation time was measured by the small-amplitude oscillation method). The solution density was $\rho = 1.303 \pm 0.03$ g cm⁻³. The inflow of a polymer solution into the channel was generated via two inlets by compressed nitrogen gas at pressures between about

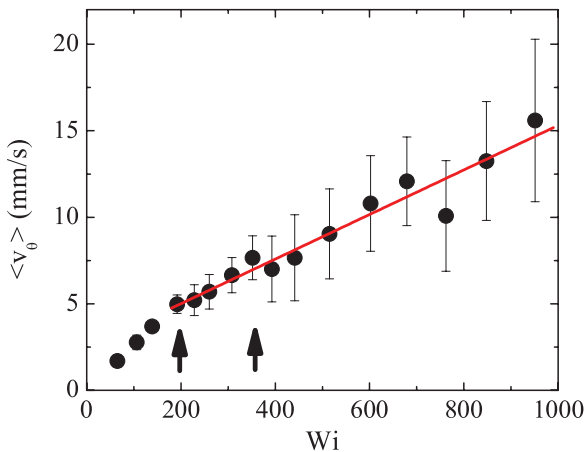


FIG. 4. (Color online) The mean longitudinal velocity at $r/d = 0.5$ as a function of Wi . Arrows indicate the elastic instability onset and the ending of a transitional regime to elastic turbulence, respectively. Solid line is a linear fit to the data.

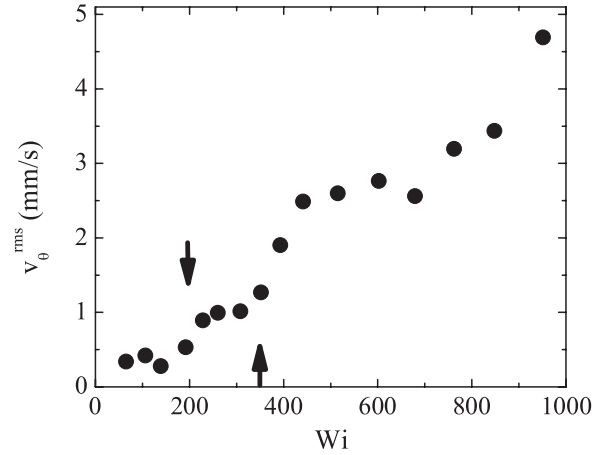


FIG. 5. Root mean square of the longitudinal velocity V_θ^{rms} versus Wi . Arrows indicate the elastic instability onset and the ending of a transitional regime to elastic turbulence, respectively.

2400 and 58 600 Pa, depending on Wi . The gas pressure was regulated and measured via a regulated pressure gauge with a precision of ± 5 Pa. The compressed gas was fed into two plastic cylinders containing a working polymer solution. The cylinders were connected to the channel inlets by Tygon tubes with inner diameter of 1.0 mm, sufficiently large to prevent a possibility of an elastic instability already in the tubes. The Weissenberg numbers $Wi = (2V_\theta^{\text{max}}/d)\lambda$ reached in the experiment by such an arrangement were in the range from 0 to 950. The maximum $Re = V_\theta^{\text{max}}d\rho/\eta$ was ~ 0.54 , so that the inertial effects in the flow were negligible, as was already shown in the earlier experiments [3–5,13].

III. PROPERTIES OF ELASTIC TURBULENCE

A. Flow structure and experimental determination of the elastic instability threshold

We searched experimentally for the onset of the elastic instability in our channel with the aspect ratio $d/R_i = 1$. In order to figure out the range of the elastic turbulence region,

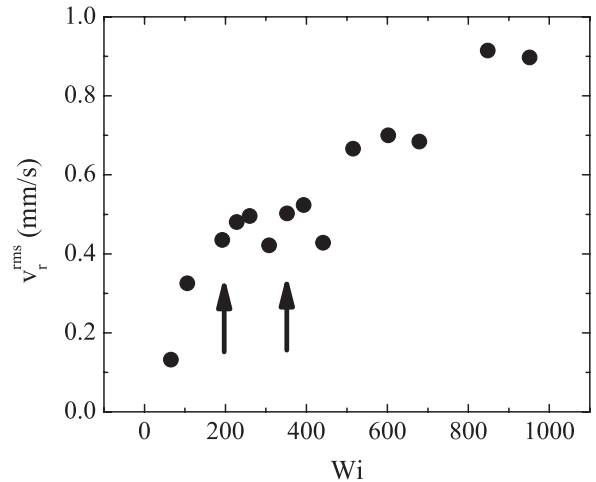


FIG. 6. Root mean square of the transversal velocity V_r^{rms} versus Wi . Arrows indicate the elastic instability onset and the ending of a transitional regime to elastic turbulence, respectively.

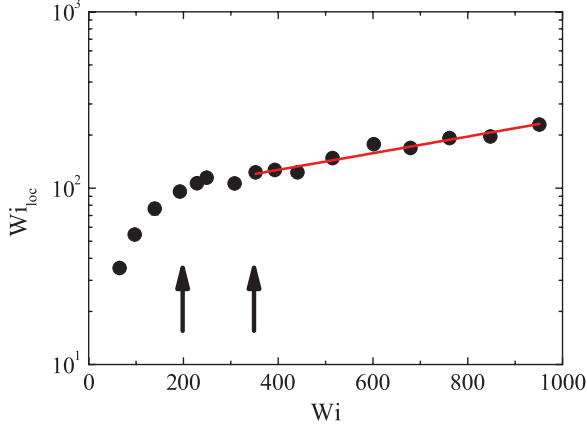


FIG. 7. (Color online) The local Weissenberg number $Wi_{loc} = (\partial V_\theta / \partial r)^{rms} \lambda$ averaged over r/d from 0.2 to 0.5 as a function of Wi . Arrows indicate the elastic instability onset and the ending of a transitional regime to elastic turbulence, respectively. The solid line is a linear fit to the data in the elastic turbulence regime.

we plot the values of $\langle V_\theta \rangle$ at $r/d = 0.5$ and V_θ^{rms} as a function of Wi in Figs. 4 and 5. From both plots one concludes that the elastic instability onset corresponds to the change in the slope that occurs at $Wi_c \simeq 200$ on the both plots. A similar change in the slope takes place in the dependence of V_r^{rms} on Wi at about the same value of Wi_c though the data is noisier (Fig. 6). An additional change in functional behavior of V_θ^{rms} and V_r^{rms} versus Wi occurs at $Wi \approx 350-400$, where the transition region to elastic turbulence is ended. The more accurate value of $Wi \simeq 350$ for this transition is determined from the plot in Fig. 5, and then the corresponding arrows indicate the onset of the elastic instability and the end of the transitional region toward elastic turbulence in all three plots in Figs. 4, 5, and 6. Thus, the range of developed elastic turbulence can be considered for Wi from about 350 up to 950.

Using the results of the PIV measurements one calculates the various components of the velocity gradient field as a function of r at different values of Wi . Figure 7 presents

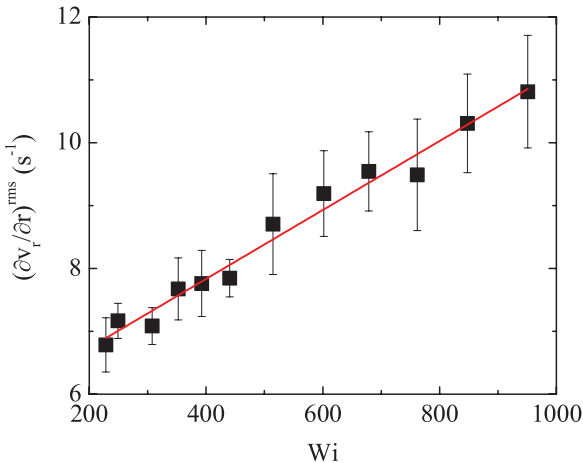


FIG. 8. (Color online) $(\partial V_r / \partial r)^{rms}$ averaged over r/d from 0.2 to 0.5 versus Wi . The solid line is a linear fit to the data $(\partial V_r / \partial r)^{rms} = (5.64 \pm 0.15) + (0.055 \pm 0.002)Wi$ in the elastic turbulence regime from $Wi = 350$ to 950.

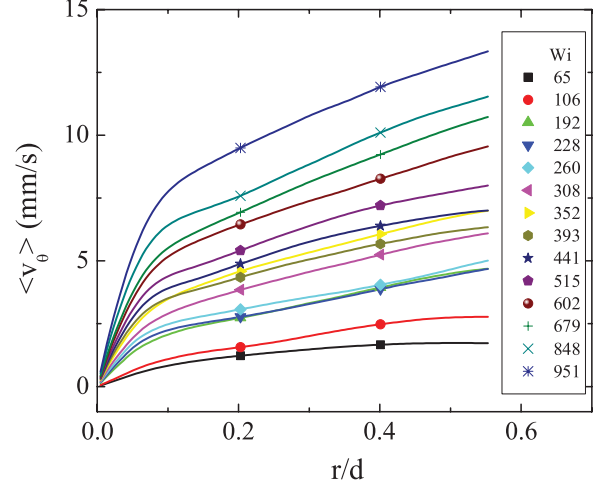


FIG. 9. (Color online) Mean longitudinal velocity profiles across the channel of a polymer solution flow for various Wi (starting from small values from bottom to top; $r = 0$ corresponds to the inner channel wall). Symbols on the curves are used as markers.

the data for $Wi_{loc} \equiv (\partial V_\theta / \partial r)^{rms} \lambda$ versus Wi averaged over r/d from 0.2 to 0.5 in the bulk flow. In the range of elastic turbulence for Wi from 350 to 950 the data in log-linear presentation in Fig. 7 are fitted by a linear fit, which gives $Wi_{loc} = 82.2 \exp(Wi/919.2)$. Figure 8 shows $(\partial V_r / \partial r)^{rms}$ averaged over r/d from 0.2 to 0.5 in the bulk flow region as a function of Wi . Here the data can be also fitted linearly by $(\partial V_r / \partial r)^{rms} = 5.64 + 0.055Wi$ in the elastic turbulence range. All PIV data were averaged over 1000 velocity fields to get both average velocity and its rms values as well as the velocity gradient components.

B. Velocity and velocity gradient profiles and the boundary layer problem

As demonstrated above, a channel flow of a polymer solution at sufficiently large Wi above the elastic instability threshold Wi_c is chaotic with large velocity fluctuations. Figure 9 shows the profiles of the average longitudinal velocity

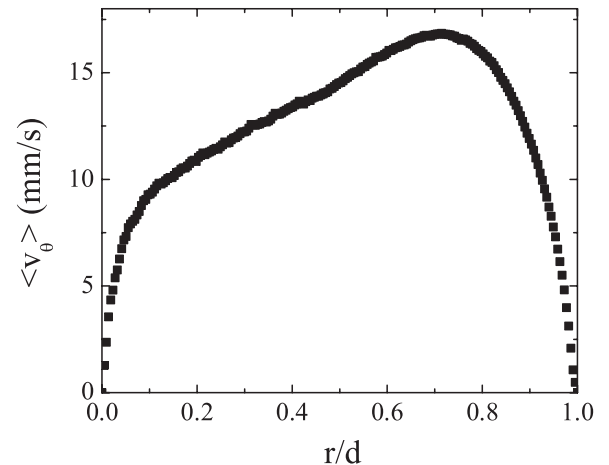


FIG. 10. The entire mean longitudinal velocity profile across the channel of a polymer solution flow for $Wi = 951$.

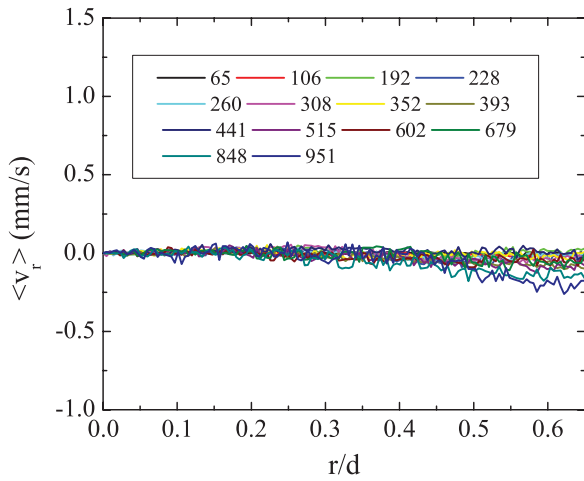


FIG. 11. (Color online) Mean transversal velocity profiles across the channel of a polymer solution flow for various Wi .

$\langle V_\theta \rangle$ across the channel for various values of Wi from below the elastic instability up to the highest values. A boundary layer characterized by a sharp drop of $\langle V_\theta \rangle$ at about $r/d \leq 0.1$ is clearly seen at Wi above 192. A full profile of $\langle V_\theta \rangle$ across the channel at $Wi = 951$ is presented in Fig. 10, where both boundary layers are clearly identified.

From the same velocity measurements the profiles of the average transversal velocity $\langle V_r \rangle$, and the rms fluctuations of the longitudinal V_θ^{rms} and transversal V_r^{rms} components of the velocity for various Wi are also obtained (see Figs. 11–13).

First, by comparing Figs. 9 and 11 one finds that $\langle V_r \rangle$ is close to zero inside the error bars across the channel, and $\langle V_\theta \rangle$ exceeds it by more than two orders of magnitude, whereas rms values of the longitudinal and transversal components are of the same order of magnitude that follows from Figs. 12 and 13. Figure 14 shows $(\partial V_\theta / \partial r)^{rms}$ versus r/d at various Wi in the whole range of its variations. Analogously, the component $(\partial V_r / \partial r)^{rms}$ as a function of r/d is plotted for various Wi

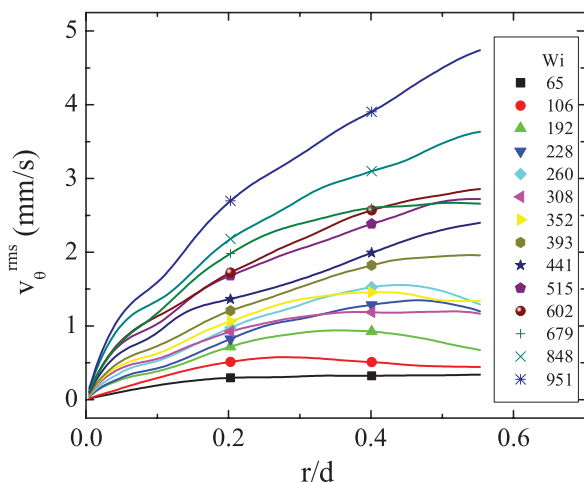


FIG. 12. (Color online) RMS fluctuations of the longitudinal velocity profiles across the channel of a polymer solution flow for various Wi (starting from small values from bottom to top; $r = 0$ corresponds to the inner channel wall). Symbols on the curves are used as markers.

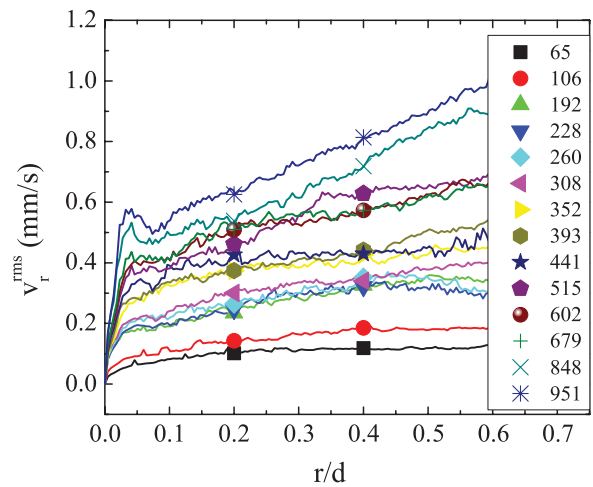


FIG. 13. (Color online) rms fluctuations of transversal velocity profiles across the channel of a polymer solution flow for various Wi (starting from small values from bottom to top; $r = 0$ corresponds to the inner channel wall). Symbols on the curves are used as markers.

in Fig. 15. As before, all PIV data were averaged over 1000 velocity fields to get both average velocity and its rms values as well as the velocity gradient components. One can see on both plots that both $(\partial V_\theta / \partial r)^{rms}$ and $(\partial V_r / \partial r)^{rms}$ approach zero values at $r/d < 0.05$, which is an artifact of low spatial resolution of the PIV images near the wall due to smaller concentration of seeding particles in the near-wall region.

Second, we present in Figs. 16 and 17 time dependencies of $V_\theta(t)$ and $V_r(t)$ in the bulk flow for the fixed value of $r/d = 0.5$ and at several values of Wi on a time interval much larger than λ . In the elastic turbulence regime at $Wi > 350$ strong fluctuations in both components of the velocity are observed.

Clearly identified in Figs. 9, 10, 14, and 15, boundary layer regions near the wall in both average velocity and rms values of both components of the velocity and velocity gradient profiles across the channel can be better studied after subtracting from each velocity profile a linear part of the profile found in the bulk region with the slope $d\langle V_\theta \rangle / dr$ (see Figs. 9 and 10) and then rescaling its value to unity. As a result, all longitudinal

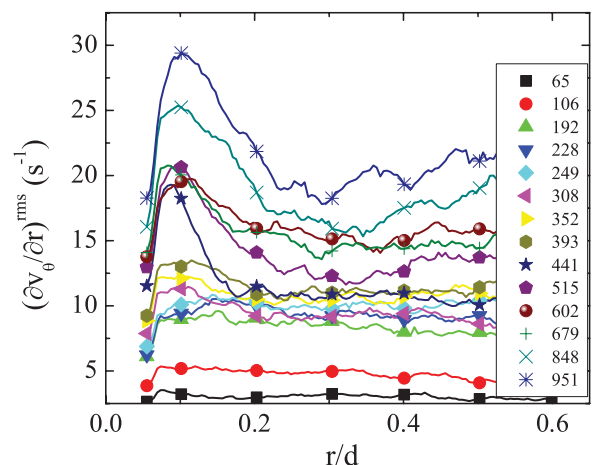


FIG. 14. (Color online) $(\partial V_\theta / \partial r)^{rms}$ versus r/d for various Wi from bottom to top. Symbols on the curves are used as markers.

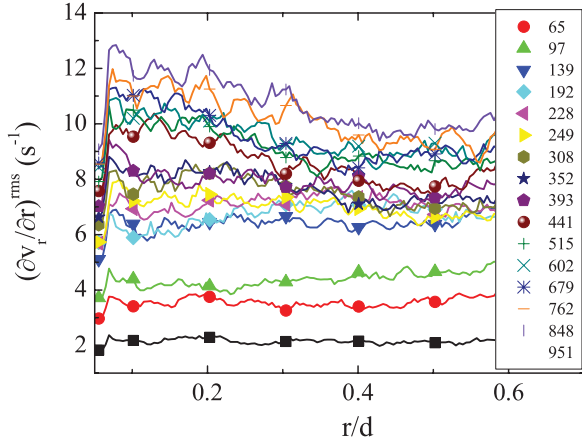


FIG. 15. (Color online) $(\partial V_r / \partial r)^{rms}$ versus r/d for various Wi from bottom to top. Symbols on the curves are used as markers.

velocity profiles at Wi in the range of elastic turbulence above 350 collapse on a single curve, demonstrating independence of the boundary layer width on Wi (Fig. 18). To get quantitative information about Wi dependence of the velocity boundary layer width l_{bl} , we fit each velocity profile, and then the values of l_{bl} as fitting parameters together with error bars present as a function of Wi in Fig. 19. The boundary layer width is independent of Wi and also Wi_{loc} (see inset in Fig. 19) and is equal $l_{bl}/d \simeq 0.1$ in a good agreement with the results obtained early in the swirling flow [7].

Finally, we present in Fig. 20 the dependencies of $(\partial V_\theta / \partial r)^{rms}$ in the bulk and and its peak values in the boundary layer regions as a function of Wi taken from the plots in Figs. 7 and 14. The peak values of $(\partial V_\theta / \partial r)^{rms}$ in the boundary layer exceed those in the bulk up to two times compared to at least an order of magnitude in the swirling flow [7,22]. This quantitative discrepancy between two flows occurs probably due to the limitation in spatial resolution of PIV on the channel width. Then the limited resolution smears out the peak value of $(\partial V_\theta / \partial r)^{rms}$.

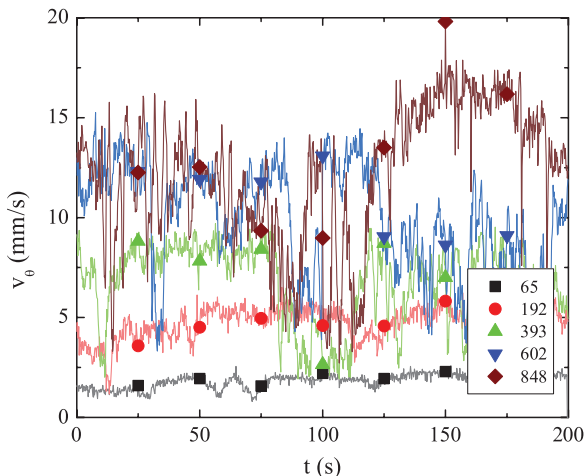


FIG. 16. (Color online) Time series of the longitudinal velocity at $r/d = 0.5$ for various Wi . Symbols on the curves are used as markers.

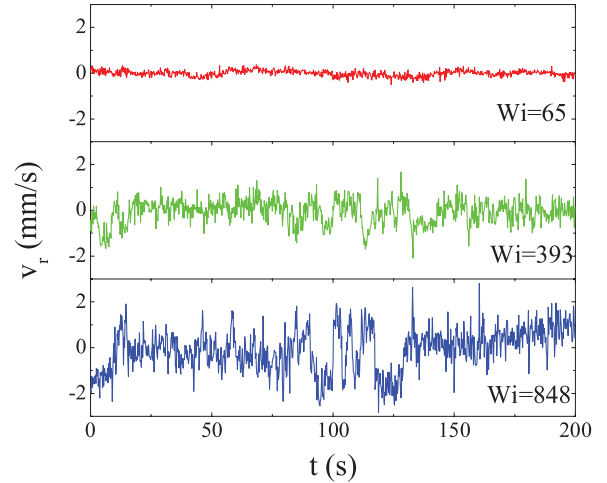


FIG. 17. (Color online) Time series of the transversal velocity at $r/d = 0.5$ for various Wi .

C. Temporal and spatial correlation functions of both velocity components and their gradients

We studied both temporal and spatial (across the channel) correlation functions of both velocity components. Figure 21 shows temporal correlation functions of the longitudinal and transversal velocity components $C(\tau) = \langle \delta V(\tau) \delta V(0) \rangle / \langle (\delta V(0))^2 \rangle$, where $\delta V_\theta(\tau) \equiv V_\theta(\tau) - \langle V_\theta \rangle$ and $\delta V_r(\tau) \equiv V_r(\tau) - \langle V_r \rangle$ at several Wi values in the elastic turbulence regime taken at the bend $N = 42$. The corresponding correlation time calculated as $\tau_{corr} = \int t C(t) dt / \int C(t) dt$ for both velocity components as a function of Wi are presented in Fig. 22. As can be seen in Fig. 22, the correlation time for $\delta V_\theta(\tau)$ is considerably larger than for $\delta V_r(\tau)$.

The spatial correlation functions $C(r/d) = \langle \delta V(r/d) \delta V(0) \rangle / \langle (\delta V(0))^2 \rangle$ and the corresponding correlation lengths for both velocity components calculated as $l_{corr}/d = \int (r/d) C(r/d) dr/d / \int C(r/d) dr/d$ are shown for several Wi in Figs. 23 and 24. Here $\delta V_\theta(r/d) \equiv V_\theta(r/d) - \langle V_\theta \rangle$ and $\delta V_r(r/d) \equiv V_r(r/d) - \langle V_r \rangle$. The correlation lengths for both components are rather

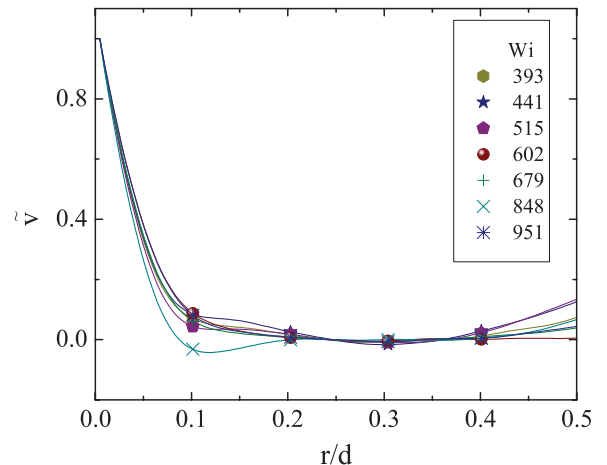


FIG. 18. (Color online) Normalized and scaled down $\langle \tilde{V}_\theta \rangle(r/d)$ velocity profiles at various Wi . Symbols on the curves are used as markers.

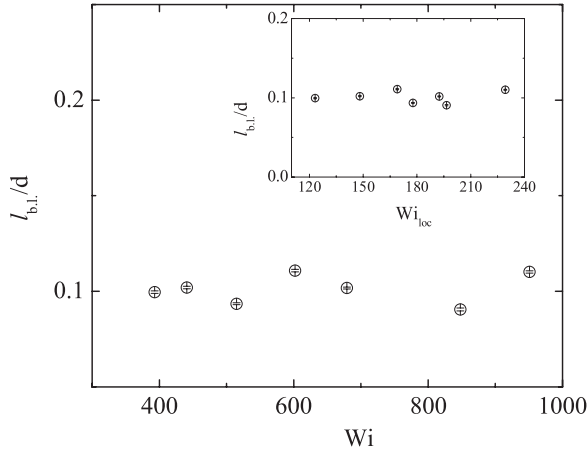


FIG. 19. Velocity boundary layer width l_{bl} versus Wi . (Inset) Velocity boundary layer width l_{bl} versus Wi_{loc} .

close and independent of Wi . Using the Taylor hypothesis one can compare the correlation lengths along the flow with those across the flow. As follows from the data in Fig. 22, the correlation time for the longitudinal component of velocity is about $\tau_{corr}/\lambda \simeq 4$ that gives for, let us say, $Wi = 600$ the normalized correlation length along the flow $\Gamma/d = \tau_{corr}\langle V_\theta \rangle \simeq 370$ that is about 2000 times larger than l_{corr}/d . Similarly, the correlation functions $\tilde{C}_\theta(r/d)$ and $\tilde{C}_r(r/d)$, as well as the corresponding correlation lengths $l_{\theta,corr}/d$ and $l_{r,corr}/d$ of the both transverse velocity gradients $\partial V_\theta/\partial r$ and $\partial V_r/\partial r$, are also calculated, and the results for different Wi were presented in Figs. 25 and 26. First, the correlation functions have minimum at $r/d \approx 0.06$ that probably corresponds to the peak location of $(\partial V_\theta/\partial r)^{rms}$ and, second, the correlation lengths are up to an order of magnitude shorter than for the velocities (see Fig. 26 versus Fig. 24) and grow with Wi .

D. Statistics of velocity gradients and their structure functions

Further verification of the scaling laws in elastic turbulence in the channel flow comes from the statistical analysis of the velocity field. We point out that the statistical analysis of the

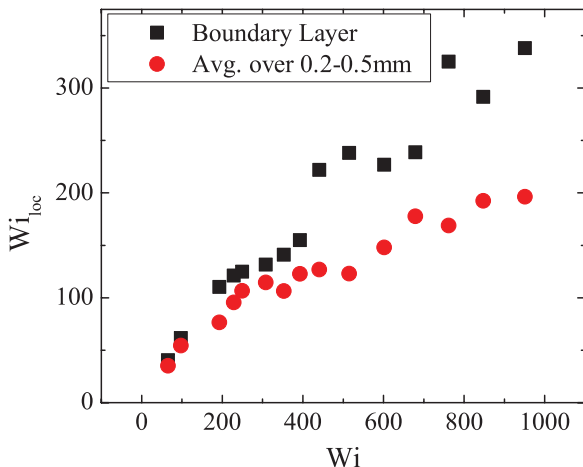


FIG. 20. (Color online) The peak values of $(\partial V_\theta/\partial r)^{rms}$ in the bulk and boundary layer versus Wi .

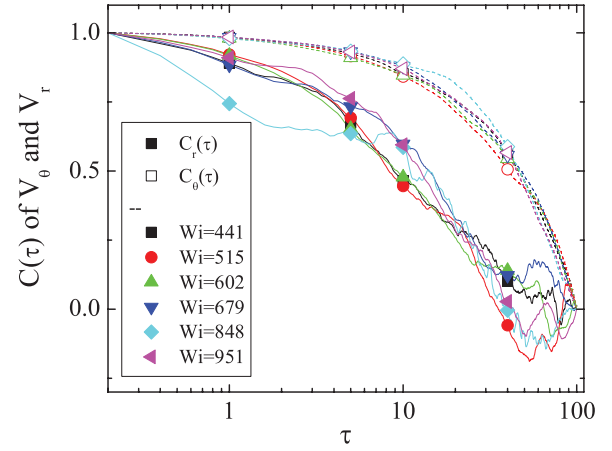


FIG. 21. (Color online) Temporal correlation functions $C_\theta(\tau)$ of $V_\theta(t)$ and temporal correlation functions $C_r(\tau)$ of $V_r(t)$, respectively, at several Wi above Wi_c taken at the bend $N = 42$. Symbols on the curves are used as markers.

longitudinal velocity component in spatial and in particular temporal domains show large scatter due to insufficient data that makes the analysis unreliable. On the other hand, the same analysis in a spatial domain of the both components of the velocity gradients exhibits much better results.

First, we conducted the statistical analysis of the spatial increments of the normalized radial gradients of the longitudinal velocity $\delta(\partial V_\theta/\partial r)/\delta(\partial V_\theta/\partial r)_{rms} \equiv [\partial V_\theta/\partial r(r/d + \delta r/d) - \partial V_\theta/\partial r(r/d)]/\delta(\partial V_\theta/\partial r)_{rms}$ in a wide range of spatial scales in increments from 9.2 to 46 μm taken with a 4.6- μm step at $Wi = 951$ for the bend $N = 42$. The corresponding probability distribution functions (PDFs) of the spatial increments of the normalized longitudinal velocity gradients $\delta(\partial V_\theta/\partial r)/\delta(\partial V_\theta/\partial r)_{rms}$ have a small Gaussian cap and show well-pronounced exponential tails, clear scale invariance, and symmetry with small scatter in spite of low statistics (see Fig. 27). Further analysis can be done in an equivalent way either by direct calculations of the structure functions or by calculations of the moments of PDFs. The corresponding second moments of PDFs $S_{2,\theta}(\delta r/d)$ as a function of $\delta r/d$ in log-log coordinates for several values of Wi show the scaling

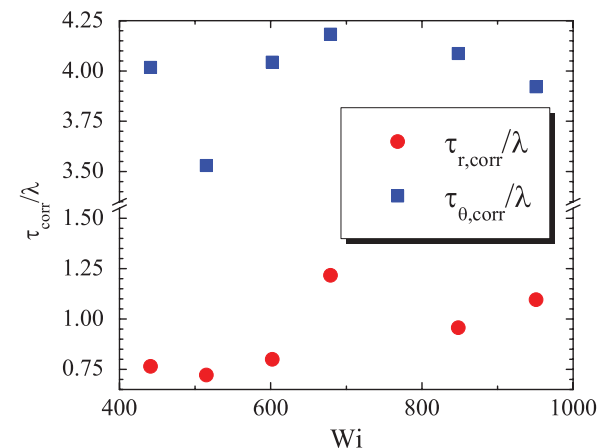


FIG. 22. (Color online) Normalized correlation times $\tau_{\theta,corr}/\lambda$ and $\tau_{r,corr}/\lambda$ versus Wi for both V_θ and V_r , respectively.

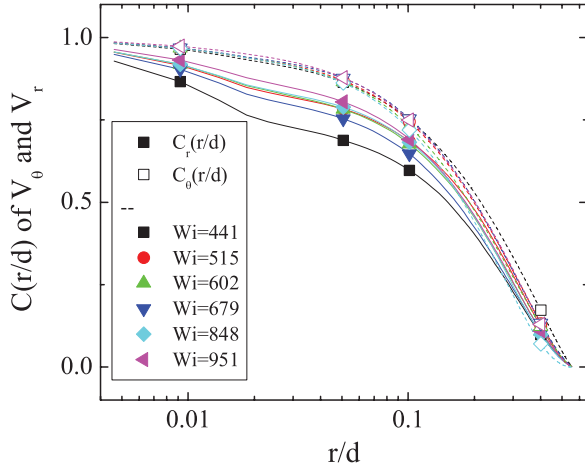


FIG. 23. (Color online) Spatial correlation functions $C_\theta(r/d)$ of $V_\theta(r/d)$ and spatial correlation functions $C_r(r/d)$ of $V_r(r/d)$, respectively, at several Wi above Wi_c taken at the bend $N = 42$. Symbols on the curves are used as markers.

region in $\delta r/d$ between 0.01 and 0.05 in Fig. 28. The structure functions of the higher even orders up to $p = 8$ $S_{p,\theta}(\delta r/d)$ as a function of $\delta r/d$ are plotted in log-log coordinates at $Wi = 951$ in Fig. 29. Due to the symmetrical shape of the PDFs odd moments are zero. The power dependence of the structure functions (or moments) $S_{p,\theta}(\delta r/d) \sim (\delta r/d)^{\zeta_{p,\theta}}$ is found in the range of $\delta r/d$ between 0.004 and 0.05. The plot in Fig. 30 demonstrates independence of the scaling exponents $\zeta_{2,\theta}$ and $\zeta_{4,\theta}$ of Wi in the whole range of elastic turbulence. The dependence of $\zeta_{p,\theta}$ is surprisingly close to the linear scaling with $\zeta_{p,\theta} = 0.75p$ shown by a solid line (see Fig. 31). The latter is very different from passive scalar behavior [14]. Analogous analysis was conducted also for the normalized radial gradients of the transverse velocity $\delta(\partial V_r/\partial r)/\delta(\partial V_r/\partial r)_{rms} \equiv [\partial V_r/\partial r(r/d + \delta r/d) - \partial V_r/\partial r(r/d)]/\delta(\partial V_r/\partial r)_{rms}$. The obtained results were very similar to the normalized radial gradient of the longitudinal velocity component. The corresponding PDFs also exhibit similar features: small Gaussian cap, exponential tails (though not so clean), scale invariance, and symmetry (see Fig. 32). As a result, the second $S_{2,r}(\delta r/d)$ and higher order even moments

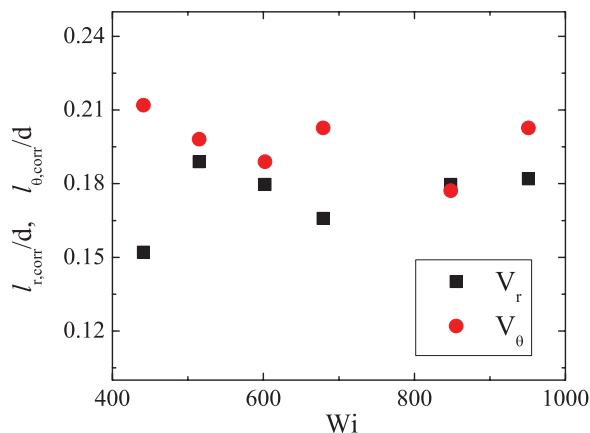


FIG. 24. (Color online) Normalized correlation length $l_{\theta,corr}/d$ and $l_{r,corr}/d$ versus Wi for both V_θ and V_r , respectively.

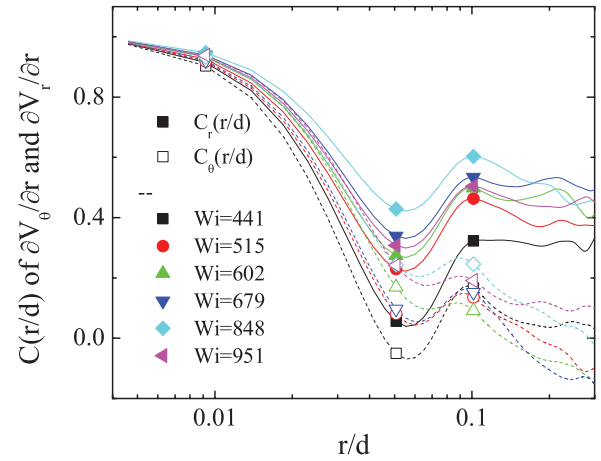


FIG. 25. (Color online) Spatial correlation functions $\tilde{C}_\theta(r/d)$ of $\partial V_\theta/\partial r$ and spatial correlation functions $\tilde{C}_r(r/d)$ of $\partial V_r/\partial r$, respectively, at several Wi above Wi_c taken at the bend $N = 42$. Symbols on the curves are used as markers.

$S_{p,r}(\delta r/d)$ (or structure functions) up to $p = 8$ show scaling in the same range of scales (Figs. 33–35), and the dependencies of their scaling exponents $\zeta_{p,r}$ on Wi (see Fig. 35) and p (see Fig. 36) are close to those found for $\delta(\partial V_\theta/\partial r)/\delta(\partial V_\theta/\partial r)_{rms}$.

IV. DISCUSSION

Let us summarize the main observations reported above.

- (i) A well-defined threshold of the elastic instability in a curvilinear channel flow is identified from the dependencies of the average longitudinal velocity and rms values of the longitudinal and transverse velocity fluctuations on Wi (Figs. 4–6). The transition to an elastic turbulence regime is determined from V_θ^{rms} as well as V_r^{rms} dependencies on Wi (Figs. 5 and 6). In the elastic turbulence regime, an exponential dependence of Wi_{loc} on Wi is observed (Fig. 7).
- (ii) The profiles of the average longitudinal velocity are altered drastically in elastic turbulence compared to a laminar flow (Fig. 9). In the elastic turbulence regime, the characteristic boundary layer is clearly identified near the wall (Figs. 9 and 10). Being normalized and rescaled, all velocity profiles are collapsed on one curve with a horizontal flat part in the bulk

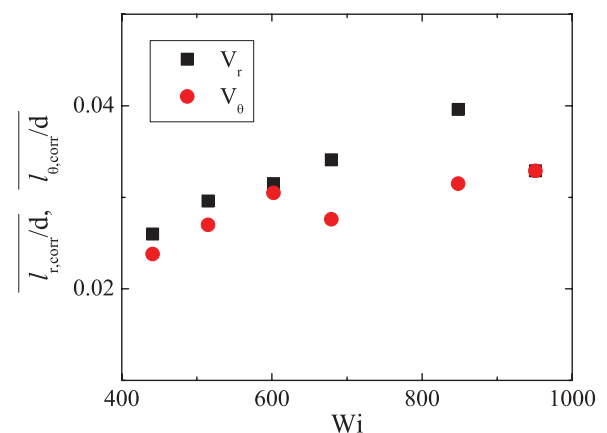


FIG. 26. (Color online) Normalized correlation length $l_{\theta,corr}/d$ and $l_{r,corr}/d$ versus Wi for both $\partial V_\theta/\partial r$ and $\partial V_r/\partial r$, respectively.

and sharp change near the wall, so that all profiles have the same boundary layer width independent of Wi , which is equal $l_{bl}/d \simeq 0.1$ (Figs. 18 and 19). (iii) On the other hand, a profile of $(\partial V_\theta/\partial r)^{rms}$ (Fig. 14) shows a peak closer to the wall, inside the velocity boundary layer discussed above, whose location near the channel wall is also independent of Wi . As we discussed in our early papers on elastic turbulence in a swirling flow [6,7], the peak in $(\partial V_\theta/\partial r)^{rms}$ means also the maximum in elastic stresses, and so the boundary layer is defined by the nonuniform spatial distribution of the elastic stresses across the channel. (iv) The correlation times determined from the temporal correlation functions for both velocity components differ up to 5 times. The correlation time for the transversal velocity component $\tau_{r,corr}$ is of the order of the polymer relaxation time, whereas the correlation time of the longitudinal velocity component $\tau_{\theta,corr}$ is several times larger (Figs. 21 and 22). (v) The correlation lengths found from the spatial correlation functions of the both velocity components are $l_{corr}/d \approx 0.18$ in the elastic turbulence regime (Figs. 23 and 24). On the other hand, the correlation lengths obtained from the spatial correlation functions of the radial gradients of the longitudinal and transversal velocity components are up to an order of magnitude smaller than for the velocity components in the whole range of elastic turbulence (Figs. 25 and 26). (vi) PDFs of the spatial increments of the radial gradients of the longitudinal and transversal velocity components in a wide range of length scales up to the boundary layer width demonstrate the scale invariance and exponential tails (Figs. 27 and 32). It is very much reminiscent of the properties of the PDFs of passive scalar mixing in the Batchelor regime studied in elastic turbulence of the curvilinear flow of a polymer solution [14]. On the other hand, the second and higher order even moments of the PDFs, contrary to the passive scalar logarithmic dependence on spatial scales, show an algebraic increase (Figs. 28–30 and 33–35) with the spatial increment and with the scaling exponents $\zeta_{p,\theta}$

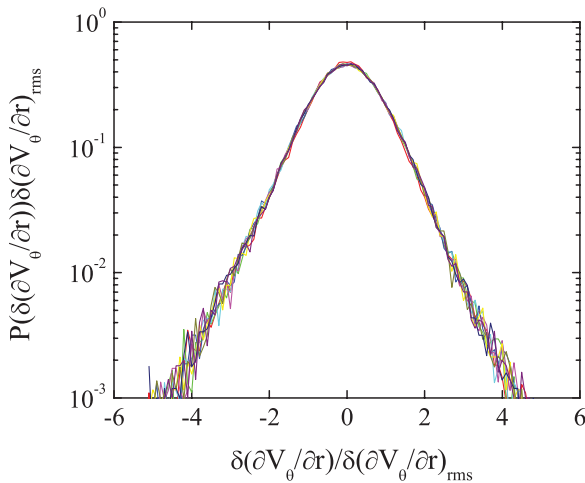


FIG. 27. (Color online) PDFs of the spatial increments of the normalized longitudinal velocity radial gradient $\delta(\partial V_\theta/\partial r)/\delta(\partial V_\theta/\partial r)_{rms} = [\partial V_\theta/\partial r(r/d + \delta r/d) - \partial V_\theta/\partial r(r/d)]/\delta(\partial V_\theta/\partial r)_{rms}$ at different length scales (from 9.2 to 46 μm with a step of 4.6 μm) at $Wi = 951$ based on its spatial velocity field measurements for the bend $N = 42$.

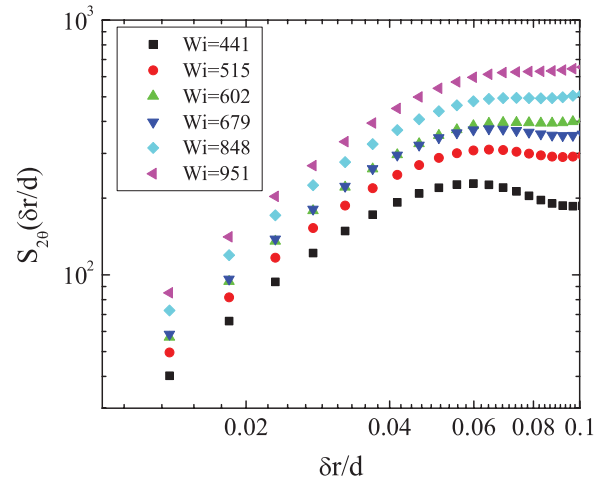


FIG. 28. (Color online) Second moments $S_{2,\theta}(\delta r/d)$ of PDFs of the longitudinal velocity gradient increments $\delta(\partial V_\theta/\partial r)$ versus $\delta r/d/\delta(\partial V_\theta/\partial r)_{rms}$ for several values of Wi (in log-log coordinates).

$\zeta_{p,r}$, where dependence on p mildly deviates from a linear one (Figs. 31 and 36).

There are several important messages which follow from the observations summarized above. (i) The elastic instability transition in a curvilinear channel is a continuous one (forward bifurcation) as already found in our early experiments [4,5,13], in contrast to those observed in Couette-Taylor [4] and swirling flows [4,7]. (ii) Contrary to the predictions, Wi_{loc} grows with Wi in the elastic turbulence regime and its value exceeds that theoretically predicted by more than two orders of magnitude. (iii) The profiles of the average longitudinal velocity component reveal the emergence of a boundary layer whose width is independent of Wi in the whole range of elastic turbulence. Being scaled by the channel width, it is also independent on the characteristic size of the system and equal $l_{bl}/d \simeq 0.1$. Both the existence of the boundary layer and the independence of its width on the control parameters of the flow are rather surprising features, in particular, if one

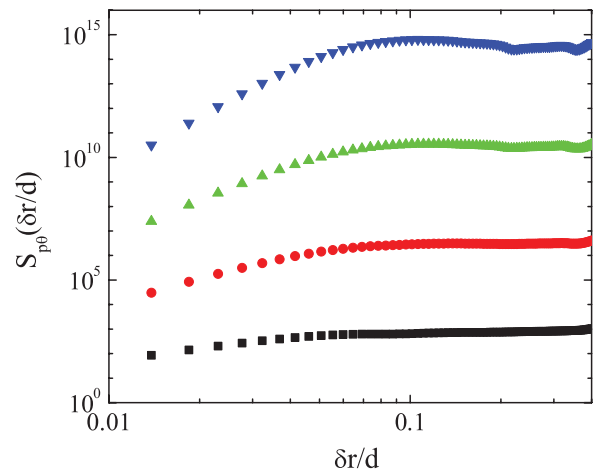


FIG. 29. (Color online) Structure functions $S_{p,\theta}(\delta r/d)$ of the longitudinal velocity gradient spatial increments $\delta(\partial V_\theta/\partial r)/\delta(\partial V_\theta/\partial r)_{rms}$ up to $p = 8$ (only even) for $Wi = 951$ (in log-log coordinates).

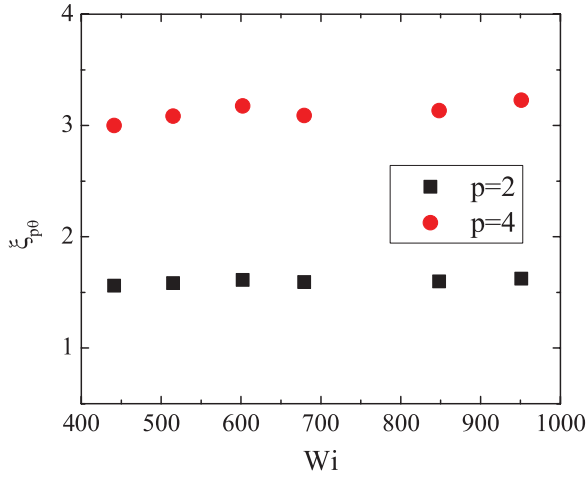


FIG. 30. (Color online) Scaling exponents of the second $S_{2,\theta}(\delta r/d)$ and fourth $S_{4,\theta}(\delta r/d)$ moments of the longitudinal velocity gradient increments $\delta(\partial V_\theta/\partial r)/\delta(\partial V_\theta/\partial r)_{\text{rms}}$ for various Wi .

takes into account that the channel width is smaller than the dissipation scale, the only characteristic inner scale of a flow defined by the dissipation rate and viscosity. This fact was already reported in Refs. [6,7] for the swirling flow. (iv) The boundary layer observed in the average velocity profiles is a reflection of a nonuniform distribution of the rms values of the radial gradient of the longitudinal velocity fluctuations. Indeed, the latter profiles exhibit more intricate behavior with sharp peaks inside the velocity boundary layer, whose locations are independent of Wi but the peak values grow with Wi . Since $(\partial V_\theta/\partial r)^{\text{rms}}$ controls the degree of polymer stretching in a random flow and in this way the elastic stress, one concludes that a similar nonuniform distribution of the elastic stresses can be expected near the wall in elastic turbulence. Direct measurement of the elastic stress is a subject for future experiments.

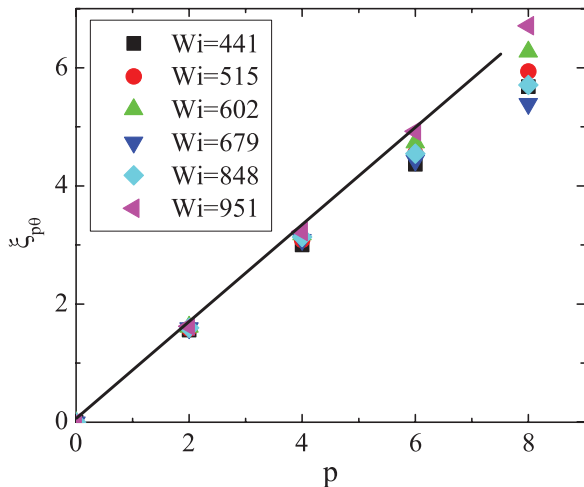


FIG. 31. (Color online) Scaling exponents $\zeta_{p,\theta}$ of the structure functions of the longitudinal velocity gradient spatial increments $\delta(\partial V_\theta/\partial r)/\delta(\partial V_\theta/\partial r)_{\text{rms}}$ versus p for various Wi . The solid line is $\zeta_{p,\theta} = 0.75p$.

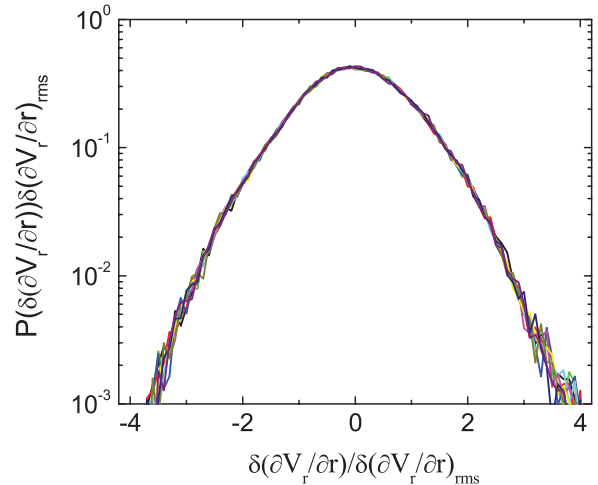


FIG. 32. (Color online) PDFs of the spatial increments of the normalized transversal velocity radial gradient $\delta(\partial V_r/\partial r)/\delta(\partial V_r/\partial r)_{\text{rms}} = [\partial V_r/\partial r(r/d + \delta r/d) - \partial V_r/\partial r(r/d)]/\delta(\partial V_r/\partial r)_{\text{rms}}$ at different length scales from 9.2 to 46 μm with a step of 4.6 μm at $Wi = 951$ based on its spatial velocity field measurements for the bend $N = 42$.

The nonuniform distribution of the elastic stresses across the channel and appearance of the characteristic spatial scales of the order of the boundary layer width of both velocity and velocity gradient in the spatial correlation functions of the velocity and velocity gradient fields in a bulk flow suggest that rare and strong parcels of excessive elastic stresses, concentrated in the boundary layer, are ejected into the bulk flow, similar to jets in passive scalar mixing in elastic turbulence observed recently [13,14,23]. The rare and strong ejection of jets of excessive passive scalar occurs in the diffusion boundary layer and protrudes into the peripheral region and even further into the bulk of the channel flow [14,24,25]. These jets considerably alter mixing and significantly reduce mixing efficiency. Similarly, in such a way the elastic stresses are introduced into the flow. This suggestion is also supported

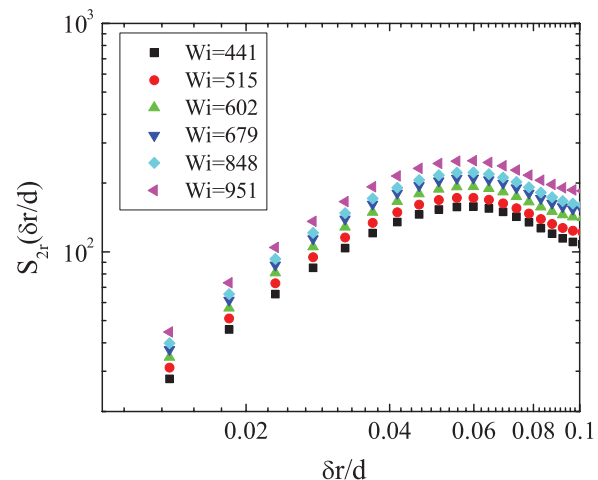


FIG. 33. (Color online) Second moments $S_{2,r}(\delta r/d)$ of PDFs of the transversal velocity gradient increments $\delta(\partial V_r/\partial r)/\delta(\partial V_r/\partial r)_{\text{rms}}$ versus $\delta r/d$ for several values of Wi (in log-log coordinates).

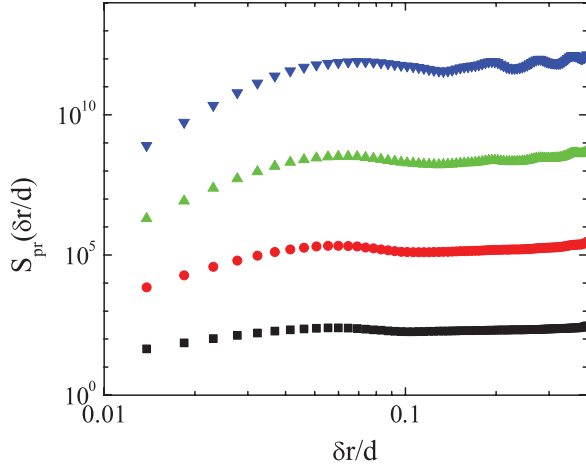


FIG. 34. (Color online) Structure functions $S_{p,r}(r/d)$ of the transversal velocity gradient increments $\delta(\partial V_r/\partial r)/\delta(\partial V_r/\partial r)_{\text{rms}}$ up to $p = 6$ (only even) for $Wi = 951$ (in log-log coordinates).

by the observations of rare and strong spikes in torque and pressure measurements in the swirling flow of a polymer solution in elastic turbulence regime [7,8]. (v) Since elastic turbulence is a smooth random flow, where only a few large spatial scale modes dominate the dynamics, one expects that l_{corr} should be of the order of d . We find in the experiment that the correlation length of the velocity field l_{corr} is about twice larger than the velocity boundary layer l_{bl} and much smaller than the channel width d . Moreover, the correlation length defined from the correlation function of the velocity gradients $\widetilde{l}_{\text{corr}}$ is about an order of magnitude smaller than l_{corr} , which relates it to the characteristic spatial scale corresponding to the peak location of $(\partial V_\theta/\partial r)^{\text{rms}}$ near the wall inside the velocity boundary layer width. Then, due to possible eruption of jets of elastic stresses, this characteristic scale is also observed in the bulk. (vi) The same range of spatial scales is found in the scaling region of the structure functions of the velocity gradients S_p , which once more indicates a possible influence

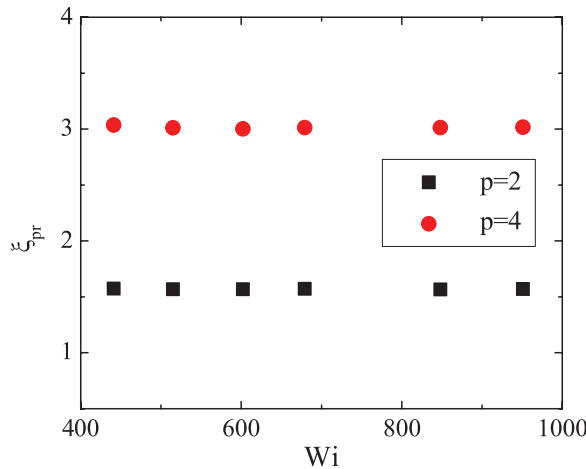


FIG. 35. (Color online) Scaling exponents of the second $S_{2,r}(\delta r/d)$ and fourth $S_{4,r}(\delta r/d)$ moments of the transversal velocity gradient increments $\delta(\partial V_r/\partial r)/\delta(\partial V_r/\partial r)_{\text{rms}}$ for various Wi .

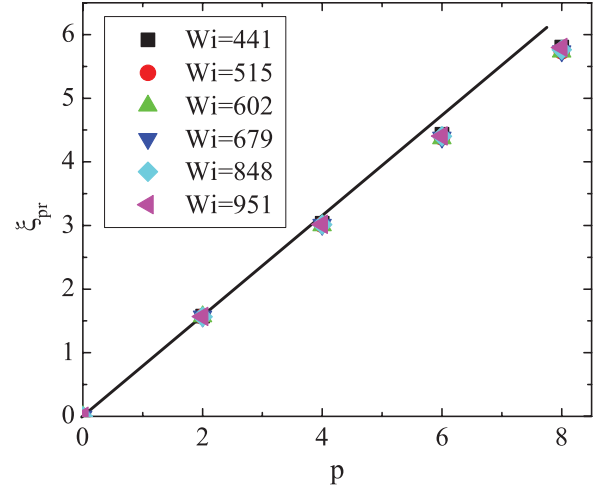


FIG. 36. (Color online) Scaling exponents $\zeta_{p,r}$ of the structure functions of the transversal velocity gradients increments $\delta(\partial V_r/\partial r)/\delta(\partial V_r/\partial r)_{\text{rms}}$ versus p for various Wi . The solid line is $\zeta_{p,\theta} = 0.75p$.

of jets protruding from the boundary layer into the bulk of the flow.

V. CONCLUSIONS

To conclude, the experimental results show that one of the main predictions of the theory of elastic turbulence, namely, the saturation of Wi_{loc} in the bulk flow of elastic turbulence, contradicts the experimental observations both qualitatively and quantitatively in spite of the fact that the theory explains quantitatively well the observed sharp power-law decay of the velocity power spectrum [9,15]. The nonuniform distribution of $(\partial V_\theta/\partial r)^{\text{rms}}$ across the channel points out the nonuniform distribution of elastic stresses. The latter may lead to the rare and strong eruption of the jets of elastic stresses from the boundary layer, where the excess of the elastic stresses is found, into the bulk and in this way to the introduction of small spatial scales into the bulk flow corresponding to the correlation lengths. This suggestion is based on the analogy with dynamics of a passive scalar near the wall in elastic turbulence in a curvilinear channel flow of a polymer solution [14]. It is also supported by the observed rare and strong drops in the torque and pressure measurements in von Karman swirling flow in the elastic turbulence regime of polymer solutions [7,8]. The existence of the resulting velocity boundary layer width and its peculiar properties observed in the experiment require a proper theoretical description. Thus, the experimental findings call for further development of a theory of elastic turbulence in a bounded container, similar to what was done for the passive scalar problem [23].

ACKNOWLEDGMENTS

This work is supported by grants from Israel Science Foundation and Lower Saxony Ministry of Science and Culture Cooperation Grant.

- [1] R. B. Bird *et al.*, *Dynamics of Polymer Liquids* (Wiley, New York, 1987).
- [2] A. Groisman and V. Steinberg, *Nature (London)* **405**, 53 (2000).
- [3] A. Groisman and V. Steinberg, *Nature (London)* **410**, 905 (2001).
- [4] A. Groisman and V. Steinberg, *New J. Phys.* **6**, 29 (2004).
- [5] T. Burghelea, E. Segre, I. Bar-Joseph, A. Groisman, and V. Steinberg, *Phys. Rev. E* **69**, 066305 (2004).
- [6] T. Burghelea, E. Segre, and V. Steinberg, *Phys. Rev. Lett.* **96**, 214502 (2006).
- [7] T. Burghelea, E. Segre, and V. Steinberg, *Phys. Fluids* **19**, 053104 (2007).
- [8] Y. Jun and V. Steinberg, *Phys. Rev. Lett.* **102**, 124503 (2009).
- [9] A. Fouxon and V. Lebedev, *Phys. Fluids* **15**, 2060 (2003).
- [10] S. Berti, A. Bistagnino, G. Boffetta, A. Celani, and S. Musacchio, *Phys. Rev. E* **77**, 055306(R) (2008).
- [11] S. Berti and G. Boffetta, *Phys. Rev. E* **82**, 036314 (2010).
- [12] H. Yatou, *Phys. Rev. E* **82**, 036310 (2010).
- [13] T. Burghelea, E. Segre, and V. Steinberg, *Phys. Rev. Lett.* **92**, 164501 (2004).
- [14] Y. Jun and V. Steinberg, *Phys. Fluids* **22**, 123101 (2010).
- [15] E. Balkovsky, A. Fouxon, and V. Lebedev, *Phys. Rev. E* **64**, 056301 (2001).
- [16] G. K. Batchelor, *J. Fluid Mech.* **5**, 113 (1959).
- [17] E. Balkovsky, A. Fouxon, and V. Lebedev, *Phys. Rev. Lett.* **84**, 4765 (2000).
- [18] M. Chertkov, *Phys. Rev. Lett.* **84**, 4761 (2000).
- [19] S. Gerashchenko, C. Chevillard, and V. Steinberg, *Europhys. Lett.* **71**, 221 (2005).
- [20] Y. Liu and V. Steinberg, *Europhys. Lett.* **90**, 44002 (2010).
- [21] Y. Liu, Y. Jun, and V. Steinberg, *J. Rheol. (Melville, NY, US)* **53**, 1069 (2009).
- [22] Y. Jun and V. Steinberg (unpublished).
- [23] M. Chertkov and V. Lebedev, *Phys. Rev. Lett.* **90**, 034501 (2003).
- [24] A. Chernykh and V. Lebedev, *JETP Lett.* **87**, 682 (2008).
- [25] H. Salman and P. H. Haynes, *Phys. Fluids* **19**, 067101 (2007).